ACS APPLIED MATERIALS & INTERFACES

Research Article

www.acsami.org

Recyclable Magnetic Mesoporous Nanocomposite with Improved Sensing Performance toward Nitrite

Yihe Zhang,[†,‡] Zisheng Su,[†] Bin Li,[*,†] Liming Zhang,[*,†] Di Fan,[†] and Heping Ma[†]

[†]State Key Laboratory of Luminescence and Applications, Changchun Institute of Optics Fine Mechanics and Physics, Chinese Academy of Sciences, Changchun 130033, P. R. China

[‡]University of Chinese Academy of Sciences, Beijing 100039, P. R. China

Supporting Information

ABSTRACT: A magnetic nanomaterial for nitrite ion detection was demonstrated in the present study. This nanomaterial was prepared by grafting a rhodamine 6G derivative (denoted as Rh 6G—OH) into the channels of core−shell magnetic mesoporous silica nanospheres. The nanocomposite (denoted as Fe_3O_4@Rh 6G) showed large surface area and improved fluorescent performance to accumulate and recognize NO_2^-, and its superparamagnetic behavior played an important role in reusability. The fluorescent intensity decreased linearly along with the NO_2^- concentration in the range of 1−50 μM, and the detection limit was estimated to be 0.8 μM, which was much lower than the maximum limit of nitrite ion in drinking water (65 μM) recommended by World Health Organization. Importantly, Fe_3O_4@Rh 6G could be magnetically collected and effectively reutilized after six test cycles.

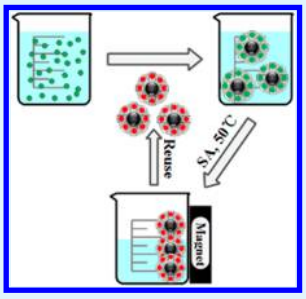

KEYWORDS: *NO_2^- sensing, nanocomposite, fluorescence, magnetism, rhodamine derivative, reutilization*

1. INTRODUCTION

Nitrite ion (NO_2^-) is widely present in environmental and food systems as an inorganic artificial fertilizer for plants and a food preservative for meat or pickle products. It could be generated during food decomposition as well.[1−3] However, a high level of nitrite brings eutrophication and hidden hazards for ecological and physiological systems.[4] Pathological researchers have connected nitrite ions with a large amount of medical diseases including "blue baby syndrome", spontaneous abortions, methemoglobinemia, and gastric cancer.[5−7] Consequently, a motivation to determine NO_2^- in various samples has been sparked.

Several analytical techniques have been reported for nitrite determination, including spectrophotometry, electrochemical method, chromatography, and capillary electrophoresis.[8−11] These techniques provide low detection limits and wide linear ranges. Nevertheless, most of them require professional equipment, complicated operation, and expensive staff, which is not suitable for online or in-field monitoring.[12] In recent years, luminescence sensing is more popular due to its remarkable advantages such as low price, highly efficient, easy handling, and convenient tracking.[13,14] Most research, however, focuses only on the design and synthesis of sensors, ignoring their recycling and reuse, which limits their practical application. In previous works, rhodamine-based nanoparticles for NO_2^- detection have been reported.[15−17] Unfortunately, the difficult reutilization, unsatisfactory response time, and detection limit still require further improvement. Hence, nanomaterials are desired because of their improved physical and chemical performance over single-component counterparts.

During the past decade, many functional materials combined with magnetic Fe_3O_4 nanoparticles have been extensively applied in various fields ranging from catalysts, magnetic resonance imaging (MRI), drug delivery carriers, and so on.[18−20] In the family of magnetic materials, magnetic mesoporous silica nanospheres with magnetically responsive core and functional shell are believed to have important advantages as follows. In the first place, nonporous silica acts as a protector, both protecting Fe_3O_4 from surrounding environmental impact and avoiding the fluorescent quenching effect caused by Fe_3O_4.[21,22] In the next place, their ordered mesoporous structure with large surface area provides an enhanced reaction zone and an amplified modify interface.[23] Third, their magnetic property makes it possible to control the process in the magnetic field and convenient to be recycled and reused via unique chemical reaction.[24−26]

Herein, we propose a novel nitrite ion detecting sensor, i.e., Fe_3O_4@Rh 6G, using nonporous silica-coated Fe_3O_4 nanospheres as core, mesoporous silica as shell, and a rhodamine derivative as probe, respectively. Our nanocomposite is fully characterized and investigated, and its sensing performance toward nitrite ion is also studied. These results show that the Fe_3O_4@Rh 6G has improved sensing ability toward nitrite ion and can be collected and reused.

2. EXPERIMENTAL SECTION

2.1. Materials and Reagents. Iron(III) chloride hexahydrate ($FeCl_3 \cdot 6H_2O$), tetraethyl orthosilicate (TEOS), cetyltrimethylammonium bromide (CTAB), and 4-hydroxy-benzaldehyde were purchased from Sinopharm Chemical Regent Co., Ltd. Anhydrous sodium

Received: February 20, 2016
Accepted: April 26, 2016
Published: April 26, 2016

DOI: 10.1021/acsami.6b02133
ACS Appl. Mater. Interfaces 2016, 8, 12344−12351

Scheme 1. (A) Plausible Synthetic Route of Formation of Fe_3O_4@Rh 6G Core−Shell Structure; (B) Treatment and Reuse of Nitrite Ion Solution Diagram

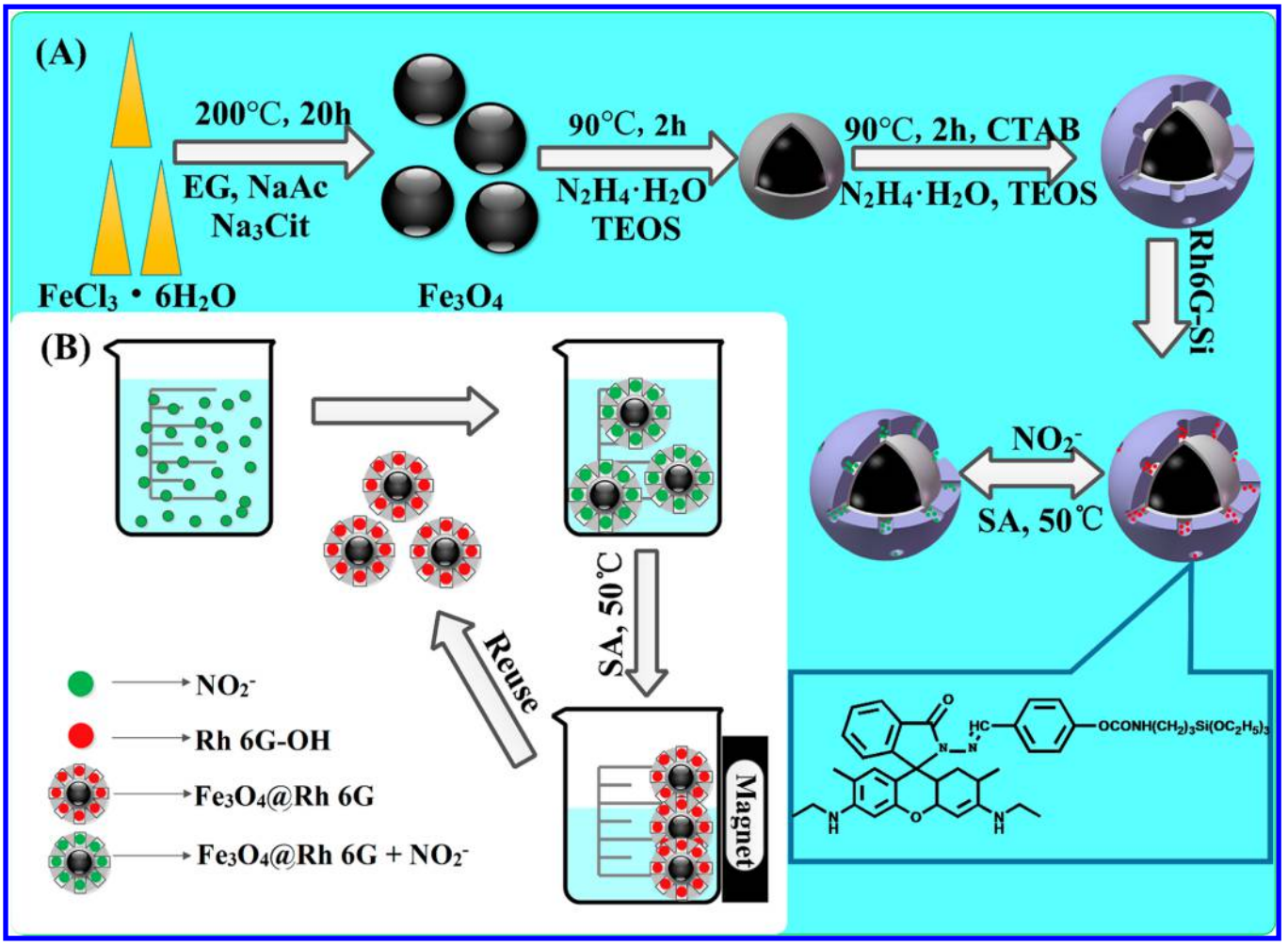

acetate (NaAc), hydrazine hydrate (85%), and triethylamine were purchased from Tianjin Fuchen Chemical Reagents Factory. 3-(Triethoxysilyl)-propyl isocyanate (TESPIC, Aldrich), sulphamic acid (SA, Shanghai Chemical Company), and rhodamine 6G (Aldrich) were used as received. Ethylene glycol, trisodium citrate (Na_3Cit), absolute ethanol, toluene, tetrahydrofuran, hexane, concentrated HCl, dichloromethane, diethyl ether, and sodium nitrite were purchased from Beijing Chemical Works. Solvent toluene, hexane, and tetrahydrofuran were first dried with activated 4A molecular sieves before use. Other analytical grade solvents and compounds were used without further purification for preparation. Deionized water was used in this work.

2.2. Preparation of Magnetic Mesoporous Silica Nanocomposite (Fe_3O_4@SiO_2). Carboxyl modified Fe_3O_4 nanoparticles were prepared following a literature procedure with trisodium citrate as surfactant.[27] Typically, $FeCl_3{\cdot}6H_2O$ (1.35 g, 5 mmol) was first dissolved in ethylene glycol (40 mL) to form a light yellow solution, then NaAc (3.6 g) and Na_3Cit (0.4 g) were added. After being stirred vigorously for 30 min, the mixture was sealed in a Teflon-lined stainless-steel autoclave (50 mL capacity). The autoclave was heated at 200 °C and maintained for 20 h. The autoclave was then cooled to room temperature. Black magnetic product was collected, washed with ethanol, and deionized water three times, and dried in vacuum at 60 °C overnight.

The core−shell structured magnetic silica nanospheres were synthesized by an improved method.[28,29] First, 0.05 g Fe_3O_4 nanoparticles were dispersed in 30 mL deionized water containing 0.5 mL of hydrazine hydrate. After being exposed to ultrasonication for 30 min, the mixture was transferred to a three-necked flask containing deionized water (70 mL). The pH was adjusted to about 9−10 by adding hydrazine hydrate, then TEOS (0.03 g) was added dropwise under mechanical stirring for 2 h at 90 °C. The product was collected through a magnet, and dispersed in deionized water (70 mL), hydrazine hydrate (0.80 mL), and CTAB (0.15 g). After being exposed to ultrasonication for 30 min, the mixture was mixed with TEOS (0.20 mL) and vigorously stirred for 2 h at 90 °C. The brownish black product was collected with centrifuge and washed with ethanol and water and dried in vacuum at 60 °C overnight. CTAB template was removed by Soxhlet extraction process: the purified microspheres (0.15 g) were dispersed in ethanol (200 mL) /acetone (15 mL) and refluxed at 90 °C for 48 h. This extraction process was repeated twice, and then these microspheres were washed with deionized water and ethanol.

2.3. Preparation of Rh 6G-Functionalized Magnetic Mesoporous Silica Nanocomposite (Fe_3O_4@Rh 6G). Rh 6G—Si was synthesized according to our previously reported method.[15] Rhodamine 6G (1.2 g, 2.5 mmol) as a starting ingredient was reacted with excess hydrazine hydrate (3 mL) and 4-hydroxy-benzaldehyde (1.22 g, 10 mmol) ethanol−dichloromethane solution (V/V = 1:2) and refluxed at 55−60 °C for 12 h. The product was recorded as Rh 6G—OH, and the yield was 68.4%. ^{1}HNMR ($CDCl_3$, 500 MHz), δ(ppm): 1.20 (t, 6H, $NHCH_2CH_3$), 1.84 (s, 6H, xanthene—CH_3), 3.07−3.18 (q, 4H, $NHCH_2CH_3$), 5.01−5.08 (b, 2H, $NHCH_2CH_3$), 6.17 (s, 2H, xanthene—H), 6.32 (s, 2H, xanthene—H), 6.73 (2H, Ben—H), 7.02 (1H, Ar−H), 7.24 (2H, Ar—H), 7.55 (2H, Ben—H), 7.87 (1H, Ar—H), 8.6 (s, 1H, N═CH), 9.89 (s, 1H, Ben—OH). Rh 6G—OH

DOI: 10.1021/acsami.6b02133
ACS Appl. Mater. Interfaces 2016, 8, 12344−12351

(0.2673 g, 0.5 mmol) was dissolved in anhydrous tetrahydrofuran (50 mL), dripped with excess TESPIC (1.25 mL, 5 mmol), and 2−5 drops of triethylamine under nitrogen atmosphere and refluxed at 66 °C for 48 h. Cold hexane was added to precipitate solid and then Rh 6G—Si was obtained. Rh 6G—Si (0.1 g) and Fe_3O_4@SiO_2 (0.1 g, 24 h at 150 °C under high vacuum) were dispersed in anhydrous toluene (50 mL) and refluxed at 110 °C for 48 h under nitrogen atmosphere. After being cooled, the product was centrifuged and adequately washed with toluene, ethanol, and acetone, respectively, to rinse away surplus Rh 6G—Si. The final product was weighted as 0.15 g and denoted as Fe_3O_4@Rh 6G.

2.4. Detection of Nitrite. In a typical detection process, 20 mg Fe_3O_4@Rh 6G was dispersed in 50 mL ethanol−water solution (V/V = 8:2) to form initial suspension. An aliquot (5 mL) of the stock suspension of Fe_3O_4@Rh 6G was added 50 mL ethanol−water solution and 3.4 mL concentrated HCl (36.5%). Then this liquid was diluted to a total volume of 100 mL with additional ethanol−water solution to give a final particle concentration of 20 mg/L with hydrogen ion concentration was 0.4 M. A freshly prepared aqueous solution of nitrite was added in the samples incrementally. The suspension was excited at 510 nm, and the emission spectra were recorded. In addition, the following peaks were measured more than 3 times, and the average values were used to determine the intensity ratio.

2.5. Apparatus and Conditions. Scanning electron microscopy (SEM) images were taken with a Hitachi S-4800 microscope. Samples were dispersed with the mixture of butyl acetate-collodion (V/V = 15:1). Transmission electron microscopy (TEM) images were measured on a JEM-2010 field-emission transmission election microscope made by Japanese JEOL Company. Powder X-ray diffraction (XRD) patterns were obtained from a Bruker D4 X-ray diffractometer (Germany) with Cu Kα_1 radiation (λ = 1.5405 Å, 40 kV, 30 mA). N_2 adsorption and desorption isotherms were tested by a Nova l000 analyzer (U.S. Quantachrome Corporation Company). Samples were degassed in vacuum at 100 °C for at least 4 h before adsorption and tested at 77 K. Surface area was calculated according to the Brunauer−Emmett−Teller (BET) equation, pore volume and pore size distribution were obtained by the Barrett−Joyner−Halenda (BJH) model. Fourier transform infrared (FTIR) spectra were investigated by a Bruker Vertex 70 FTIR spectrophotometer within 4000−400 cm^{-1} region using KBr pellet method. Thermogravimetric analysis (TGA) was measured using a Diamond DSC thermal analyzer from PerkinElmer Company. Samples were heated linearly from 40 to 600 °C under a heating rate of 10 °C/min with dry N_2 flow rate of 10 mL/min. Magnetic measurement was performed using a MPM5-XL-5 superconducting quantum interference device (SQUID) magnetometer at room temperature under a varying magnetic field from −10 kOe to 10 kOe. All fluorescence spectra were conducted by a Hitachi F-7000 fluorescence spectrophotometer with excitation and emission slits set at 5 nm.

3. RESULTS AND DISCUSSIONS

3.1. Structure and Characterization of the Magnetic Nanocomposite. The synthetic process of Fe_3O_4@Rh 6G nanocomposite, the mechanism of response of the nitrite ion, and duplicate detection are summarized schematically in Scheme 1. Fe_3O_4 nanoparticle is selected as a core due to its magnetic property. Rh 6G—OH acts as a fluorescent probe owing to its response to nitrite. The mesoporous silica shell displays both as a probe carrier and a nanoreactor.

3.1.1. Morphology of the Nanocomposite. Shape, size, and inner structure of the nanocomposite are imaged by their SEM and TEM, as shown in Figure 1a. Pure Fe_3O_4 nanoparticles have shown a spherical shape with average diameter of 170 nm. These Fe_3O_4 nanospherical are composed of many small magnetite nanocrystals (Figure 1b), which makes the material a superparamagnetic one.[30] After being coated by amorphous silica and mesoporous silica, the average diameter of Fe_3O_4@SiO_2 is increased to 250 nm, as shown in Figure 1c. Meanwhile, Fe_3O_4@SiO_2 surface appears smoother and more spherical. Through its TEM picture (Figure 1d), the inner structure is clearly identified in Fe_3O_4@SiO_2. There is only one Fe_3O_4 core in every obtained nanoparticle, with a silica shell thickness of 40 nm. Hence, its core−shell structure is confirmed. In Figure 1d, the black stripes in the shell represent the wall of mesoporous, while the white stripes in the shell represent the channel. They are both perpendicular to the Fe_3O_4 surface. The slight out of plumb may due to the angle of view. This structure is beneficial to increasing the surface area, allowing more sensing molecules to improve sensitivity.

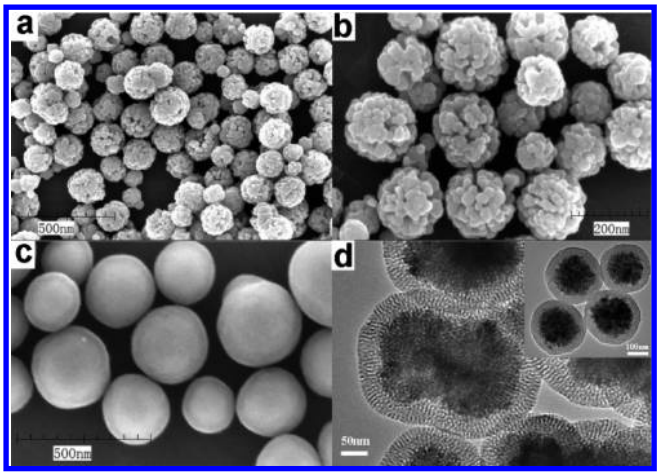

Figure 1. SEM images of the Fe_3O_4 particles before (a, b) and after (c) the silica coating, TEM images of Fe_3O_4@SiO_2 (d).

3.1.2. Nanocrystal Structure of the Inner Fe_3O_4 Core and the Outer Mesostructure. Figure S1a of the Supporting Information (SI) shows XRD patterns of our synthesized magnetic microspheres, which are nearly identical to those of spinel Fe_3O_4 nanoparticles (PDF #65-3107). Fe_3O_4@SiO_2 (Figure S1b) and Fe_3O_4@Rh 6G (Figure S1c) have shown similar patterns, as depicted by Figure S1a, illustrating that magnetite phase is well maintained after being coated with SiO_2 shell and modified with rhodamine 6G derivative. The appearance of broad peak in the range of 10−20° might attribute to the amorphous silica layer, which was not find in the pure Fe_3O_4. However, the reduced diffraction intensity after modification probably is mainly due to the reduced Fe_3O_4 ratio in our hybrid samples. According to Debye−Scherrer formula, nanocrystal size is calculated as 5 nm, which makes the material superparamagnetic.[26] In the low-angle XRD region (Figure S1 inset), there is an obvious diffraction peak at 2.3°, suggesting the existence of ordered mesoporous silica. The above result indicates that the mesoporous silica is coated on the surface of Fe_3O_4 core, providing a place for probe.

As shown in Figure 2, Fe_3O_4@SiO_2 and Fe_3O_4@Rh 6G have typical IV type curves according to IUPAC classification, which indicates that they have a highly ordered mesoporous structure. BET surface area of Fe_3O_4@SiO_2 nanoparticles is calculated to be 403.93 m^2/g, which is quite lower than that of pure mesoporous silica (more than 1000 m^2/g).[31] This lower surface area is mainly due to the Fe_3O_4 doping in Fe_3O_4@SiO_2. In addition, BET surface area, total pore volume and pore diameter of Fe_3O_4@Rh 6G (265.47 m^2/g, 0.22 cm^3/g, 2.3 nm) are all smaller than those of Fe_3O_4@SiO_2 (403.93 m^2/g, 0.68 cm^3/g, 2.7 nm) owing to the fact that sensor molecules have been grafted into mesoporous channels.

DOI: 10.1021/acsami.6b02133
ACS Appl. Mater. Interfaces 2016, 8, 12344−12351

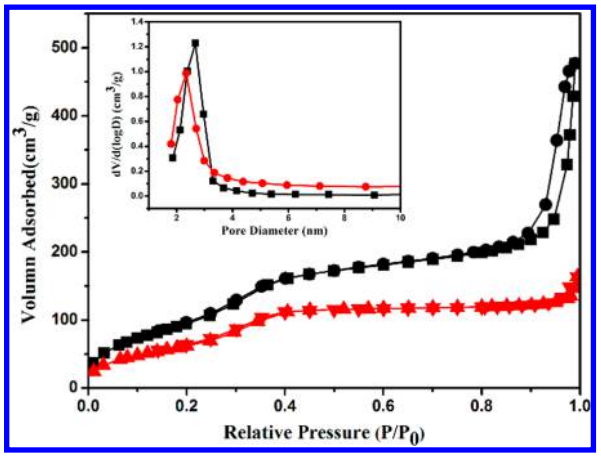

Figure 2. Nitrogen adsorption−desorption isotherms and pore size distribution (inset) of Fe_3O_4@SiO_2 (black), and Fe_3O_4@Rh 6G (red).

3.1.3. FTIR and TG Analysis. FTIR analysis has been performed on Fe_3O_4 (a), Rh 6G—OH (b), Rh 6G—Si (c), CTAB—Fe_3O_4@SiO_2 (d), Fe_3O_4@SiO_2 (e), and Fe_3O_4@Rh 6G (f). As shown in Figure S2a, the absorption band at 570 cm^{-1} is attributed to Fe—O vibration absorption and the absorption bands at 1566, 1453, 1407 cm^{-1} are caused by carboxyl group on the surface of Fe_3O_4, which increases the water solubility. In Figure S2b, the absorption band at 3442 cm^{-1} is attributed to hydroxyl vibration absorption. Rh 6G—Si exhibits a series of methylene vibration absorption bands at 2974, 2928, and 2885 cm^{-1} and amido bond at 1519, 1649 cm^{-1}, Si—O at 1101 cm^{-1}, respectively, suggesting the success of Rh 6G—OH covalent grafting with TESPIC.[15] Rh 6G—Si in this work is used as a connecting molecule, forming inorganic Si—O network structure and responding toward nitrite ion. There is no absorption in region from 2800 to 3000 cm^{-1} in Figure S2e, illustrating the successful removal of CTAB.[24] Several new bands at about 3025−2830 cm^{-1} and 1700, 1649, 1519 cm^{-1} in Figure S2f are reasonably considered as the contribution of methylene and amide groups from Rh 6G—Si. However, absorption bands at 1076 cm^{-1} (ν_{as}, Si—O), 796 cm^{-1} (ν_s, Si—O) and 457 cm^{-1} (δ, Si—O—Si) illustrate the formation of the Si—O network structure,[32] which confirms that our rhodamine probe molecules have been covalently grafted with mesoporous silica.

To calculate the content of Fe, Si, and organic probe in Fe_3O_4@Rh 6G, inductively coupled plasma optical emission spectrometry (ICP-OES), elemental analysis, and TGA have been researched. The Fe/Si molar ratio is determined by ICP, and the Fe/Si molar ratio is calculated to be 0.72. The higher ratio than the original addition quality 0.63 may be attributed to the unconnected SiO_2 having been extracted. The Rh 6G compound content is determined by elemental analysis and TG analysis. According to elemental analysis, the quality fraction of nitrogen element is measured 1.65%, which reveals that the content of Rh 6G—Si in Fe_3O_4@Rh 6G is approximately 18.4 wt %. TGA curve is delineated in Figure S3. The DTG curve (blue line) was obtained by differentiating the curve of TGA (black line), as it was difficult to distinguish the temperature range of different weight loss stages in TGA. Fe_3O_4@Rh 6G displays four stages of weight loss: (1) a small weight loss of 3.3 wt % in the range of 40−155 °C which can be attributed to the removal of physically adsorbed water and organic solvent; (2) a main weight loss of 11.2 wt % occurred at 160−380 °C (DTG_{max} = 305 °C), which is predominantly due to the decomposition of organic probe molecules; (3) the third weight loss of 6.0 wt % in region of 380−470 °C (DTG_{max} = 430 °C) which is caused by Si—C, C—C, and C—N fracture and organic silicon network structure decomposition; (4) the final weight loss 6.7 wt % in region of 470−572 °C (DTG_{max} = 516 °C), which can be assigned to the complete dehydration and deconstruction of silica framework. What is more, in region of 380−470 °C and 470−572 °C, there are two stages of weight loss, although they are not clear enough in TGA. This unconspicuous change in TGA curve is corresponding to the tiny range in DTG curve (almost 10^{-3}).[33] To sum up, the content of Rh 6G—Si in Fe_3O_4@Rh 6G is 17.2 wt % (a total weight loss of the second and the third stages), which is approximate with the elemental analysis result.

3.1.4. Magnetic Property. Magnetic hysteresis loops of Fe_3O_4 (a), Fe_3O_4@SiO_2 (b) and Fe_3O_4@Rh 6G (c) are recorded and shown in Figure 3. Their magnetization

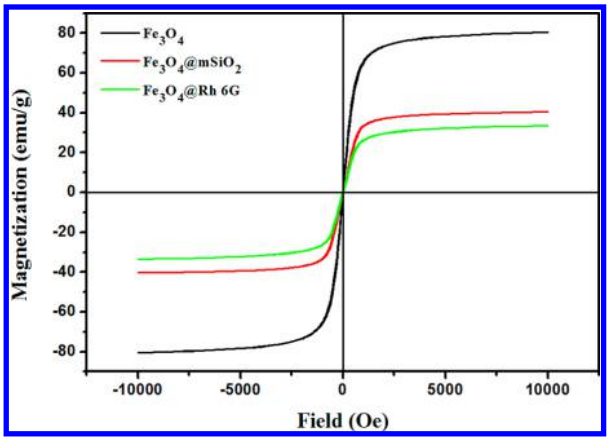

Figure 3. Magnetic hysteresis loops of pure Fe_3O_4 (black), Fe_3O_4@SiO_2 (red), Fe_3O_4@Rh 6G (green), and separation-redispersion process of Fe_3O_4@Rh 6G (inset).

saturation values are 80.4, 40.4, and 33.5 emu/g, respectively. No remanence and coercivity are obtained, suggesting that these nanoparticles are superparamagnetic ones. According to literature reports,[34,35] Fe_3O_4 nanoparticles smaller than 20−30 nm all have superparamagnetic behavior, while those larger than 30 nm may have a ferromagnetic property. We thus come to a conclusion that each Fe_3O_4 core is made up of many smaller nanocrystals. It can be observed that Fe_3O_4@Rh 6G nanoparticles are rapidly collected from homogeneously dispersed solution in less than 1 min by a magnet, and after slightly vibrating it disperses in the solvent again as illustrated in Figure 3 inset.

3.2. Optical Property and Sensing Performance of Fe_3O_4@Rh 6G. *3.2.1. Optical Property.* Figure S4 presents the fluorescence spectra of Fe_3O_4@SiO_2, Rh 6G—OH and Fe_3O_4@Rh 6G. Fe_3O_4@Rh 6G shows a characteristic emission peaking at 556 nm, showing a slight blue shift of 6 nm compared to Rh 6G—OH emission. This phenomenon can be explained by the fact that all energy levels of sensing molecules are increased in mesoporous channels as a result of their confinement effect, leading to emission light blue shift.[24] Meanwhile, this fluorescence is obviously quenched after adding nitrite ion, confirming that Rh 6G—Si is successfully grafted onto Fe_3O_4@SiO_2. This result is consistent with corresponding IR result.

DOI: 10.1021/acsami.6b02133
ACS Appl. Mater. Interfaces 2016, 8, 12344−12351

3.2.2. Acid Sensibility and Spectral Stability. In general, a rhodamine derivative shows no fluorescence in neutral or alkaline solution, whereas a strong fluorescence results in an acidic solution. Hence, acidic medium is necessary for a rhodamine sensing process. Suitable HCl concentration is consequently investigated to ensure this sensing process.[34] A series of samples, Rh 6G—OH (2.5 μM) and Fe_3O_4@Rh 6G (20 mg/L) are prepared with different HCl concentrations from 0.1 to 1.0 M. Their fluorescence response is shown in Figure 4. In order to eliminate the effects of operating error and

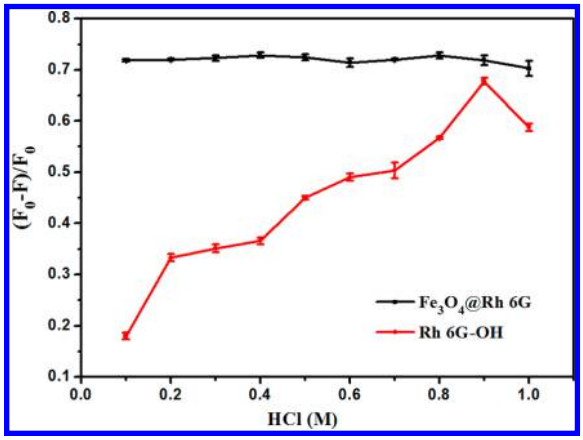

Figure 4. Variation of fluorescence intensity at 556 nm of Rh 6G—OH (red, 2.5 μM) and Fe_3O_4@Rh 6G (black, 20 mg/L) in ethanol-acidic solution (V/V = 8:2) with and without 50 μM NO_2^- to inspect the effect of HCl concentration. Excitation at 510 nm.

other factors, we researched the sensing properties with the intensity ratio in this work instead of absolute intensity. For Rh 6G—OH, HCl concentration plays an important role in the sensing process, since its quenching fluorescent ratio appears to be an obvious undulation within the range of 0.1−1.0 M. The highest ratio is 67.1% with HCl concentration of 0.9 M. However, the ratio change is limited for Fe_3O_4@Rh 6G, suggesting that acidity does not remarkably affect the sensing process after being grafted in mesoporous silica structure. This result might contribute to the hydroxyl on silica surface which can interact with protons. Notably, the fluorescent quenching ratio for Fe_3O_4@Rh 6G is higher than that for Rh 6G—OH. It is assumed that the mesoporous structure increases contacting area and NO_2^- concentration. Meanwhile, the nonporous silica shell protects the Fe_3O_4 core from acidic medium. The 0.4 M HCl concentration is proven as the optimal condition since its fluorescence quenching rate is higher than that of other HCl concentrations.

Fluorescence intensity monitoring of Fe_3O_4@Rh 6G (20 mg/L) and pure Rh 6G—OH (2.5 μM) upon 510 nm excitation under continuous radiation is depicted in Figure S5. Both Fe_3O_4@Rh 6G and pure Rh 6G—OH shows photobleaching. However, Fe_3O_4@Rh 6G stability has been greatly improved since its silica material provides a buffering environment, which protects probe molecules from light-induced structure decomposition.

3.2.3. Response Time. To display sensing rate of Fe_3O_4@Rh 6G (20 mg/L) and Rh 6G—OH (2.5 μM) toward nitrite ion, their fluorescence intensity variation is shown in Figure 5. Both fluorescence curves decline rapidly and then gradually. Fe_3O_4@Rh 6G reaction rate is slightly higher than Rh 6G—OH reaction rate. After 15 min, Fe_3O_4@Rh 6G reaction curve

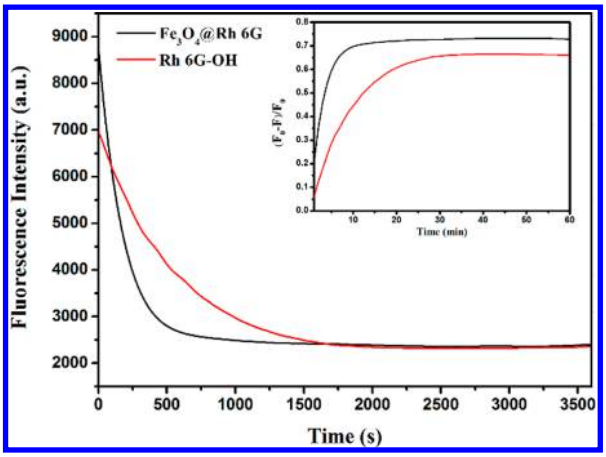

Figure 5. Fluorescence intensity time scan of Rh 6G—OH (red, 2.5 μM) and Fe_3O_4@Rh 6G (black, 20 mg/L) in the presence of NO_2^- (50 μM); relative fluorescence intensity with the change of time (inset). Excitation at 510 nm.

becomes flat and the sensing process achieves a balance. Therefore, 15 min is selected as our reaction time. This value is shorter than our previous report (35 min) since our mesoporous silica with uniform and parallel porous structure could improve analyte diffusion. However, the response time of 15 min is still long for a nanosensor. The addition of electron-rich molecules such as triphenylamine into the rhodamine probe may possibly reduce the response time.[36]

3.2.4. Response Performance of Fe_3O_4@Rh 6G toward Nitrite Ion. Fluorescence spectra of Fe_3O_4@Rh 6G (20 mg/L) with various nitrite ion concentrations are shown in Figure 6.

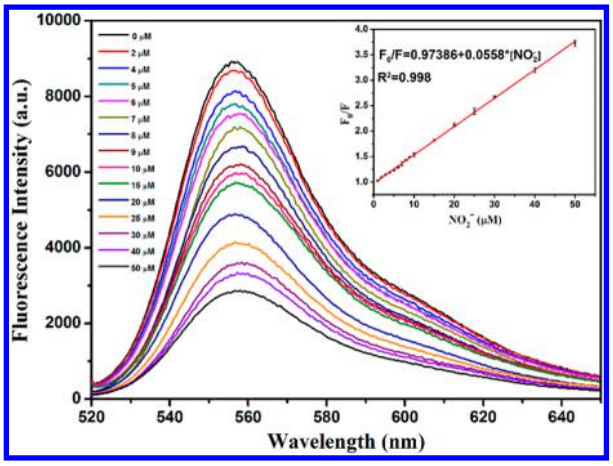

Figure 6. Fluorescence spectra changes of Fe_3O_4@Rh 6G (20 mg/L) in the presence of increasing concentration of NO_2^- in ethanol-acidic solution (V/V = 8:2). Inset: Fitting curve linearity between the nitrite ion concentration (range 1 to50 μM) and the change of Fe_3O_4@Rh 6G fluorescence intensity (F_0/F). Excitation at 510 nm.

With increasing nitrite ion concentration, Fe_3O_4@Rh 6G fluorescence is obviously quenched. This significant emission quenching could be attributed to a static quenching mechanism according to previous conclusions.[37] Interestingly, there has been no observation that the fluorescence intensity drops to zero after adding abundant nitrite. There are two possible reasons. The main reason is that the quenching mechanism between the rhodamine probe and nitrite is based on the electron-withdrawing effect, that is, NO_2^- can make the

DOI: 10.1021/acsami.6b02133
ACS Appl. Mater. Interfaces 2016, 8, 12344−12351

Table 1. Comparison of Different Nitrite Detection Methods

material	detection limit	detecting range	response time	reusability	reference
GNRs	4 μM	1−15 μM	20 min	N/A	40
MTT-GNPs	1 ppm	0−5 ppm	30 min	N/A	41
CTAB-GO/MWNT/GCE	1.5 μM	5.0−800 μM	N/A	N/A	42
BSA-AuNCs	1.0 nM	0.02−50 μM	20 min	N/A	43
U−Tb−OBBA CPNPs	0.3 μM	0.3−470 μM	N/A	N/A	44
NR-UCNPs	4.67 μM	3.32−62.5 μM	N/A	N/A	39
RB-PDA	2 μM	2−10 μM	10 min	N/A	45
Azo-based probe	0.6 μM	0.3−3.0 μM	N/A	N/A	46
Fe_3O_4@Rh 6G	0.8 μM	1−50 μM	15 min	6 cycles	this work

secondary amine group of rhodamine derivative react with itself to form a nitroso group, which quenched the fluorescence of rhodamine to some extent. But, the rhodamine derivative usually displays strong fluorescence under acidic conditions due to the structure change from spirocyclic to ring-opened. As the test condition was in acidic solution, the fluorescence intensity would not drop to zero although nitrite was added. Another possible reason may be caused by the partial rhodamine probe in the deep channel, which is not reacted with nitrite, so that a week fluorescence is remained.

A good linear response between F_0/F and NO_2^- concentration is obtained (R^2 of 0.998) as shown by Figure 6 inset. Here, we define detection limit L as $3\sigma_{bi}/m$, where σ_{bi} is the standard deviation of blank measurements, and m is the slope of working curve, respectively.[38] Our nitrite ion detection limit is calculated as 0.8 μM (0.038 ppm) using 20 mg/L Fe_3O_4@Rh 6G, far lower than the ceiling nitrite concentration in drinking water and meat products (1 and 200 ppm, respectively).[39] Such a low detection limit is mainly attributed to the large surface area of mesoporous material which accommodates more probe molecules and increases the local concentration of the nitrite ion. The detection range, limit of detection, and response time are comparable or a little better than those of other previously reported methods for nitrite, which is listed in Table 1.

3.3. Anti-interference Performance. Selectivity is one of the important indicators of sensing systems. We choose some familiar anions such as Cl^-, I^-, NO_3^-, CO_3^{2-}, and Ac^- and cations such as Mg^{2+}, Ca^{2+}, Cu^{2+}, Fe^{2+}, and Fe^{3+} as well as common proteins and organic acids such as glycine (Gly), aspartic acid (Asp), milk, and orange juice to examine their effect on Fe_3O_4@Rh 6G. Milk and orange juice were tested after the filtering procedure and their adding quantity were the same as others interferents. As shown in Figure 7, most interferents cause a slim fluorescence intensity change of Fe_3O_4@Rh6G (blue bars), only NO_2^- triggers the nitrosation reaction and shows remarkable fluorescence decline. Furthermore, when NO_2^- is added into the Fe_3O_4@Rh 6G solution with the above ions, no obvious change is observed (orange bars). The above result confirms that Fe_3O_4@Rh 6G shows a good selectivity for NO_2^- in ethanol-acidic solution (V/V = 8:2).

3.4. Reusability of Fe_3O_4@Rh 6G. Fluorescence is expected to be recovered when meeting strong reductants such as SA.[15] Reusability of Fe_3O_4@Rh 6G is evaluated by the below operation. Nitrite ion and amino sulfonic acid is sequentially introduced into the system step-by-step for several cycles, corresponding fluorescence change is examined, as shown in Figure 8. Fluorescence is rapidly quenched by nitrite addition, implementing nitrite sensing. The fluorescence

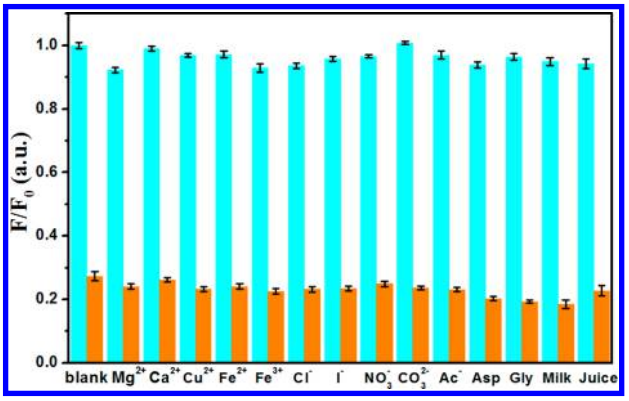

Figure 7. Relative fluorescence intensity of Fe_3O_4@Rh 6G in the presence of various interferents (100 μM) in the absence (blue bars) and presence (orange bars) of NO_2^- (50 μM). The intensities were recorded at 556 nm, excitation at 510 nm.

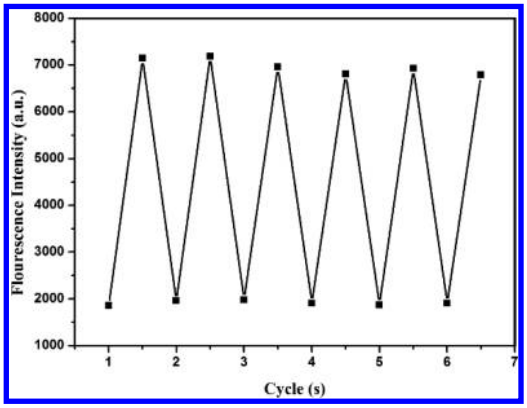

Figure 8. Fluorescence responses of Fe_3O_4@Rh 6G (20 mg/L) by alternate addition in 50 μM of NO_2^- and 100 mM of SA. The cyclic index is the number of alternating immersing/rinsing cycles. Excitation at 510 nm.

intensity can be fully recovered by amino sulfonic acid. But this fluorescence recovery needs to be heated to 50 °C. The compared fluorescence intensity with the original emission implied that the combination of rhodamine probe and Fe_3O_4@SiO_2 is stable. There is barely leakage during measurement in acidic media and recovering using amino sulfonic acid. The Fe_3O_4 core in Fe_3O_4@Rh 6G makes it separable through a magnet, and its sensing ability is well remained after six cycles. Comparison of the sensing performance of this method with some other previous works demonstrating Fe_3O_4@Rh 6G had good reusability, which has not been founnd in other nitrite sensors (Table 1).

DOI: 10.1021/acsami.6b02133
ACS Appl. Mater. Interfaces 2016, 8, 12344−12351

Table 2. Determination of Nitrite in Real Water Samples

samples	standard addition (μM)	detected amount (μM)	recovery (%)	RSD (%) (n = 3)
deionized water	2.0	1.88 ± 0.068	94.0	2.5
	5.0	4.90 ± 0.036	98.0	1.2
	8.0	8.08 ± 0.15	101	3.2
tap water	2.0	2.04 ± 0.058	102.0	2.1
	5.0	4.94 ± 0.092	98.8	2.5
	8.0	8.21 ± 0.18	102.6	3.7

3.5. Application in Real Samples. To assess the feasibility of our method, real water samples including tap water are testified, as shown in Table 2. Nitrite is detected in real water samples, with no obvious difference between the obtained results and the standard addition concentrations. The quantitative recoveries of nitrite range from 94.0% to 102.6%, confirming that Fe_3O_4@Rh 6G could be applied in real samples.

4. CONCLUSIONS

To summarize, a facile preparation of functionalized magnetic mesoporous nanomaterial was constructed by grafting a rhodamine 6G derivative into the channels of monodisperse core−shell magnetic mesoporous spheres. The introduction of magnetic mesoporous matrix significantly improved sensing performance and reusability. This composite material exhibited improved sensing performance with limited photobleaching, short response time (15 min), and low detection limit of nitrite ion (0.8 μM). Furthermore, over 95% of the original sensing signal could be recovered after six cycles. The above result demonstrated that this material was reliable and practical in applications, which made it a promising candidate for nitrite ion detection in water, food, and environment.

■ ASSOCIATED CONTENT

Supporting Information

The Supporting Information is available free of charge on the ACS Publications website at DOI: 10.1021/acsami.6b02133.

XRD, FTIR, TG analysis, fluorescence spectra, and spectrum stability (PDF)

■ AUTHOR INFORMATION

Corresponding Authors

*E-mail: libinteacher@163.com (B.L.).
*E-mail: Zhanglm770@163.com (L.Z.).

Notes

The authors declare no competing financial interest.

■ ACKNOWLEDGMENTS

The authors gratefully thank the financial supports of the NSFC (Grant Nos. 51372240, 51572256, and 21501166).

■ REFERENCES

(1) Yu, Q.; Ma, J.; Zou, P.; Lin, H.; Sun, W.; Yin, J.; Fu, J. Effects of combined application of organic and inorganic fertilizers plus nitrification inhibitor DMPP on nitrogen runoff loss in vegetable soils. *Environ. Sci. Pollut. Res.* **2015**, *22*, 472−481.
(2) Vilian, A. T.; Veeramani, V.; Chen, S. M.; Madhu, R.; Kwak, C. H.; Huh, Y. S.; Han, Y. K. Immobilization of myoglobin on Au nanoparticle-decorated carbon nanotube/polytyramine composite as a mediator-free H_2O_2 and nitrite biosensor. *Sci. Rep.* **2015**, *5*, 18390.
(3) Kumar, V. V.; Anthony, S. P. Highly selective silver nanoparticles based label free colorimetric sensor for nitrite anions. *Anal. Chim. Acta* **2014**, *842*, 57−62.
(4) Jiao, S.; Jin, J.; Wang, L. One-pot preparation of Au-RGO/PDDA nanocomposites and their application for nitrite sensing. *Sens. Actuators, B* **2015**, *208*, 36−42.
(5) Jaiswal, S. K.; Mandal, D.; Visweswara Rao, R. V. R. L. Recovery and reuse of nitric acid from effluents containing free nitric acid in absence and presence of metal nitrates. *Chem. Eng. J.* **2015**, *266*, 271−278.
(6) Wang, D. M.; Lin, H. Y.; Shah, S. I.; Ni, C. Y.; Huang, C. P. Indirect electrochemical reduction of perchlorate and nitrate in dilute aqueous solutions at the Ti-water interface. *Sep. Purif. Technol.* **2009**, *67*, 127−134.
(7) Chetty, A. A.; Prasad, S. Flow injection analysis of nitrate and nitrite in commercial baby foods. *Food Chem.* **2016**, *197*, 503−508.
(8) Zhao, J.; Lu, Y.; Fan, C.; Wang, J.; Yang, Y. Development of a cloud point extraction and spectrophotometry-based microplate method for the determination of nitrite in human urine and blood. *Spectrochim. Acta, Part A* **2015**, *136*, 802−807.
(9) Haldorai, Y.; Kim, J. Y.; Vilian, A. T. E.; Heo, N. S.; Huh, Y. S.; Han, Y. K. An enzyme-free electrochemical sensor based on reduced graphene oxide/Co_3O_4 nanospindle composite for sensitive detection of nitrite. *Sens. Actuators, B* **2016**, *227*, 92−99.
(10) Lopez Moreno, C.; Perez, I. V.; Urbano, A. M. Development and validation of an ionic chromatography method for the determination of nitrate, nitrite and chloride in meat. *Food Chem.* **2016**, *194*, 687−694.
(11) Kalaycıoğlu, Z.; Erim, F. B. Simultaneous Determination of Nitrate and Nitrite in Fish Products with Improved Sensitivity by Sample Stacking-Capillary Electrophoresis. *Food Anal. Method.* **2016**, *9*, 706−711.
(12) Wang, W.; Leng, J.; Yu, Y.; Lu, L.; Bai, L.; Qiu, X. An electropolymerized rhodamine B sensing film-based electrochemical sensor for nitrite with high sensitivity and selectivity. *Int. J. Electrochem. Sc.* **2014**, *9*, 921−930.
(13) Lutsyk, P.; Arif, R.; Hruby, J.; Bukivskyi, A.; Vinijchuk, O.; Shandura, M.; Yakubovskyi, V.; Kovtun, Y.; Rance, G. A.; Fay, M.; Piryatinski, Y.; Kachkovsky, O.; Verbitsky, A.; Rozhin, A. A sensing mechanism for the detection of carbon nanotubes using selective photoluminescent probes based on ionic complexes with organic dyes. *Light: Sci. Appl.* **2016**, *5*, e16028.
(14) Zhou, P.; Zhou, D.; Tao, L.; Zhu, Y.; Xu, W.; Xu, S.; Cui, S.; Xu, L.; Song, H. 320-fold luminescence enhancement of $[Ru(dpp)_3]Cl_2$ dispersed on PMMA opal photonic crystals and highly improved oxygen sensing performance. *Light: Sci. Appl.* **2014**, *3*, e209.
(15) Wang, L.; Li, B.; Zhang, L.; Zhang, L.; Zhao, H. Fabrication and characterization of a fluorescent sensor based on Rh 6G-functionlized silica nanoparticles for nitrite ion detection. *Sens. Actuators, B* **2012**, *171−172*, 946−953.
(16) Liao, F.; Song, X.; Yang, S.; Hu, C.; He, L.; Yan, S.; Ding, G. Photoinduced electron transfer of poly(o-phenylenediamine) - Rhodamine B copolymer dots: application in ultrasensitive detection of nitrite in vivo. *J. Mater. Chem. A* **2015**, *3*, 7568−7574.
(17) Wu, Y.-C.; Nie, F. A core−shell structured nanocomposite modified with rhodamine derivative for nitrite ion sensing. *Sens. Actuators, B* **2015**, *212*, 120−126.

DOI: 10.1021/acsami.6b02133
ACS Appl. Mater. Interfaces 2016, 8, 12344−12351

(18) Sun, W.; Yang, W.; Xu, Z.; Li, Q.; Shang, J. K. Synthesis of Superparamagnetic Core-Shell Structure Supported Pd Nanocatalysts for Catalytic Nitrite Reduction with Enhanced Activity, No Detection of Undesirable Product of Ammonium, and Easy Magnetic Separation Capability. *ACS Appl. Mater. Interfaces* **2016**, *8*, 2035−2047.
(19) Papasimakis, N.; Thongrattanasiri, S.; Zheludev, N. I.; García de Abajo, F. J. The magnetic response of graphene split-ring metamaterials. *Light: Sci. Appl.* **2013**, *2*, e78.
(20) Vivek, R.; Thangam, R.; Kumar, S. R.; Rejeeth, C.; Sivasubramanian, S.; Vincent, S.; Gopi, D.; Kannan, S. HER2 Targeted Breast Cancer Therapy with Switchable ″Off/On″ Multifunctional ″Smart″ Magnetic Polymer Core-Shell Nanocomposites. *ACS Appl. Mater. Interfaces* **2016**, *8*, 2262−2279.
(21) Zhang, Y.; Pan, S.; Teng, X.; Luo, Y.; Li, G. Bifunctional Magnetic−Luminescent Nanocomposites: Y2O3/Tb Nanorods on the Surface of Iron Oxide/Silica Core−Shell Nanostructures. *J. Phys. Chem. C* **2008**, *112*, 9623−9626.
(22) Gai, S.; Yang, P.; Li, C.; Wang, W.; Dai, Y.; Niu, N.; Lin, J. Synthesis of Magnetic, Up-Conversion Luminescent, and Mesoporous Core-Shell-Structured Nanocomposites as Drug Carriers. *Adv. Funct. Mater.* **2010**, *20*, 1166−1172.
(23) Martínez-Máñez, R.; Sancenón, F.; Hecht, M.; Biyikal, M.; Rurack, K. Nanoscopic optical sensors based on functional supramolecular hybrid materials. *Anal. Bioanal. Chem.* **2011**, *399*, 55−74.
(24) Liu, R.; Guo, Y.; Odusote, G.; Qu, F.; Priestley, R. D. Core-shell Fe_3O_4 polydopamine nanoparticles serve multipurpose as drug carrier, catalyst support and carbon adsorbent. *ACS Appl. Mater. Interfaces* **2013**, *5*, 9167−9171.
(25) Floess, D.; Chin, J. Y.; Kawatani, A.; Dregely, D.; Habermeier, H.-U.; Weiss, T.; Giessen, H. Tunable and switchable polarization rotation with non-reciprocal plasmonic thin films at designated wavelengths. *Light: Sci. Appl.* **2015**, *4*, e284.
(26) Wang, Y.; Li, B.; Zhang, L.; Li, P.; Wang, L.; Zhang, J. Multifunctional Magnetic Mesoporous Silica Nanocomposites with Improved Sensing Performance and Effective Removal Ability toward Hg(II). *Langmuir* **2012**, *28*, 1657−1662.
(27) Liu, J.; Sun, Z.; Deng, Y.; Zou, Y.; Li, C.; Guo, X.; Xiong, L.; Gao, Y.; Li, F.; Zhao, D. Highly Water-Dispersible Biocompatible Magnetite Particles with Low Cytotoxicity Stabilized by Citrate Groups. *Angew. Chem., Int. Ed.* **2009**, *48*, 5875−5879.
(28) Deng, Y.; Qi, D.; Deng, C.; Zhang, X.; Zhao, D. Superparamagnetic High-Magnetization Microspheres with an Fe_3O_4@SiO_2 Core and Perpendicularly Aligned Mesoporous SiO_2 Shell for Removal of Microcystins. *J. Am. Chem. Soc.* **2008**, *130*, 28−29.
(29) Zou, J.; Peng, Y. G.; Tang, Y. Y. A facile bi-phase synthesis of Fe_3O_4@SiO_2 core-shell nanoparticles with tunable film thicknesses. *RSC Adv.* **2014**, *4*, 9693−9700.
(30) Deng, H.; Li, X.; Peng, Q.; Wang, X.; Chen, J.; Li, Y. Monodisperse Magnetic Single-Crystal Ferrite Microspheres. *Angew. Chem., Int. Ed.* **2005**, *44*, 2782−2785.
(31) Kresge, C. T.; Leonowicz, M. E.; Roth, W. J.; Vartuli, J. C.; Beck, J. S. Ordered mesoporous molecular sieves synthesized by a liquid-crystal template mechanism. *Nature* **1992**, *359*, 710−712.
(32) Nikoorazm, M.; Ghorbani-Choghamarani, A.; Mahdavi, H.; Esmaeili, S. M. Efficient oxidative coupling of thiols and oxidation of sulfides using UHP in the presence of Ni or Cd salen complexes immobilized on MCM-41 mesoporous as novel and recoverable nanocatalysts. *Microporous Mesoporous Mater.* **2015**, *211*, 174−181.
(33) Li, J.; Yang, C.; Wu, Y.; Wang, B.; Sun, W.; Shao, T. A strategy for optical site-specific oxygen sensing: Construction and characterization of a Ru(II)-modified magnetic-luminescent hybrid composite. *Inorg. Chim. Acta* **2016**, *441*, 1−8.
(34) Ge, J.; Hu, Y.; Biasini, M.; Beyermann, W. P.; Yin, Y. Superparamagnetic Magnetite Colloidal Nanocrystal Clusters. *Angew. Chem., Int. Ed.* **2007**, *46*, 4342−4345.
(35) Xu, X.; Deng, C.; Gao, M.; Yu, W.; Yang, P.; Zhang, X. Synthesis of Magnetic Microspheres with Immobilized Metal Ions for Enrichment and Direct Determination of Phosphopeptides by Matrix-Assisted Laser Desorption Ionization Mass Spectrometry. *Adv. Mater.* **2006**, *18*, 3289−3293.
(36) Yang, Y.; Li, B.; Zhang, L.; Li, P.; Jiang, H. Multi-branched triphenylamine-rhodamine derivatives: synthesis and fluorescent sensing for Cu^{2+} and Hg^{2+} ions. *Talanta* **2013**, *115*, 938−942.
(37) Dhanya, S.; Joy, J.; Rao, T. P. Fabrication and characterization of rhodamine 6G entrapped sol-gel film test strip for virtually specific and sensitive sensing of nitrite. *Sens. Actuators, B* **2012**, *173*, 510−516.
(38) Neupane, L. N.; Kim, J. M.; Lohani, C. R.; Lee, K.-H. Selective and sensitive ratiometric detection of Hg^{2+} in 100% aqueous solution with triazole-based dansyl probe. *J. Mater. Chem.* **2012**, *22*, 4003−4008.
(39) Han, J.; Zhang, C.; Liu, F.; Liu, B.; Han, M.; Zou, W.; Yang, L.; Zhang, Z. Upconversion nanoparticles for ratiometric fluorescence detection of nitrite. *Analyst* **2014**, *139*, 3032−3038.
(40) Chen, Z.; Zhang, Z.; Qu, C.; Pan, D.; Chen, L. Highly sensitive label-free colorimetric sensing of nitrite based on etching of gold nanorods. *Analyst* **2012**, *137*, 5197−5200.
(41) Nam, Y. S.; Noh, K. C.; Kim, N. K.; Lee, Y.; Park, H. K.; Lee, K. B. Sensitive and selective determination of NO_2^- ion in aqueous samples using modified gold nanoparticle as a colorimetric probe. *Talanta* **2014**, *125*, 153−158.
(42) Yang, Y. J.; Li, W. CTAB functionalized graphene oxide/multiwalled carbon nanotube composite modified electrode for the simultaneous determination of ascorbic acid, dopamine, uric acid and nitrite. *Biosens. Bioelectron.* **2014**, *56*, 300−306.
(43) Liu, H.; Yang, G.; Abdel-Halim, E. S.; Zhu, J. J. Highly selective and ultrasensitive detection of nitrite based on fluorescent gold nanoclusters. *Talanta* **2013**, *104*, 135−139.
(44) Le Natur, F.; Calvez, G.; Freslon, S.; Daiguebonne, C.; Bernot, K.; Guillou, O. Extending the lanthanide−terephthalate system: Isolation of an unprecedented Tb(III)-based coordination polymer with high potential porosity and luminescence properties. *J. Mol. Struct.* **2015**, *1086*, 34−42.
(45) Xue, Z.; Wu, Z.; Han, S. A selective fluorogenic sensor for visual detection of nitrite. *Anal. Methods* **2012**, *4*, 2021.
(46) Chatterjee, A.; Khandare, D. G.; Saini, P.; Chattopadhyay, A.; Majik, M. S.; Banerjee, M. Amine functionalized tetraphenylethylene: a novel aggregation-induced emission based fluorescent chemodosimeter for nitrite and nitrate ions. *RSC Adv.* **2015**, *5*, 31479−31484.

DOI: 10.1021/acsami.6b02133
ACS Appl. Mater. Interfaces 2016, 8, 12344−12351